The final publication is available at

http://dx.doi.org/10.1016/j.enconman.2012.07.009

Additional Information

Study of hysteretic thermoelectric behavior in photovoltaic materials using the finite element method, extended thermodynamics and inverse problems

R. Palma[a], J.L. Pérez-Aparicio[a], R. Bravo[b]

[a]*Mecánica de Medios Continuos y Teoría de Estructuras, Universitat Politècnica de València, Spain*
[b]*Structural Mechanics & Hydraulic Engineering, University of Granada, Spain*

Abstract

The main objective of the present work is to develop and prove a theoretical explanation based on the Extended Non-Equilibrium Thermodynamics (ENET) for the hysteretical thermoelectric behavior observed in certain thin-film photovoltaic materials. The ENET introduces dissipative fluxes in the entropy balance that could explain this behavior. To verify this explanation from a numerical point of view, results are generated using a Finite Element (FE) formulation based on the ENET and already developed in previous publications by the authors. In addition, an identification Inverse Problem (IP) is formulated; a cost function is defined as the quadratic difference between experimental and numerical results and the IP is solved minimizing the cost function and using genetic algorithms. The conclusion is that the loop-like distributions are due to energy dissipation introduced by dissipative fluxes that are closely related with relaxation times. Also, the FE-IP combination permits to find an approximated characterization of properties for several materials from single experimental curves. Finally, several numerical simulations are proposed for laboratory experiments to further validate the theoretical interpretation and to confirm the relation between relaxation times and hysteresis.

Keywords: Thin-film, Thermoelectric, Hysteresis, Finite Element Method, Extended Thermodynamics, Relaxation times, Inverse problems

1. Introduction

Thin-film semiconductors have drawn great attention in the last two decades due to their suitability, among other applications, for cells in solar energy. Semiconductors of the thermoelectric type are completely characterized by their figure-of-merit, that depends on thermal and electric conductivities and on the *Seebeck* coefficient. These properties must be determined experimentally to characterize the semiconductors and to design the solar cells themselves.

An experimental study for the measurement of the *Seebeck* coefficient in thin-film semiconductors has been published in [1], reporting a hysteretic behavior that prevents correct and unique measurements of this coefficient. In [2], a similar behavior was observed in the cuticle of the oriental hornet *Vespa Orientalis*. This cuticle seemly works as a thermoelectric heat pump for the cooling of the hornet body, and as a solar energy harvesting allowing the hornet to increase its activity in the presence of strong insolation, [3].

A theoretical and a practical challenge emerge from these works:

i) Physical interpretation of the hysteretic behavior

ii) Measurement of the *Seebeck* coefficient

The first was undertaken in the references, concluding that the reason for this behavior could lay in ferroelectric properties (polarization phenomena). Pyroelectric interactions were discarded in [1]. According to [4], the reason could be related with the heating and cooling speeds during the measurement process. For the second challenge, an empirical procedure without sound theoretical basis was proposed in [1], consisting on an analytical fitting of the experimental curves. Another alternative was proposed in [2], measuring the *Seebeck* coefficient uniquely at the heating branch.

In the present work we state that from a physics theoretical point of view and using the Extended Non-Equilibrium Thermodynamics (ENET) [5], hysteretic phenomena are due to the presence of multiple thermodynamic configurations accessible to the thermodynamic system; these metastable configurations are

closely related with relaxation times, [6]. The ENET assumes the existence of a non–equilibrium entropy density that depends on the classical state variables and on the dissipative fluxes, in a formulation defined as thermodynamic mixed. This theory permits the study of thermodynamic systems for which the local equilibrium hypothesis is not valid, introducing relaxation times in the formulation.

We aim to undertake the two aforementioned challenges, studying them with the Finite Element (FE) formulation based on ENET developed in [7], along with classical Inverse Problem (IP) techniques. Experiments for several materials performed in [1] are numerically replicated, and in addition a Sensitivity Analysis complemented by an IP is developed. In particular the FE-IP combination is employed for the characterization of the *Seebeck* coefficient and, in the future, for the efficiency optimization of solar cells. Finally, three numerical experiments for the verification of the ENET-based explanation are discussed and proposed for laboratory verification.

2. Theoretical formulation

The thermoelectric balance equations are the balance of energy and of electric charge [8]:

$$\rho_m c \, \dot{T} = -\nabla \cdot \boldsymbol{q} - \boldsymbol{j} \cdot \nabla V \; ;$$

$$\nabla \cdot \boldsymbol{j} = 0 \tag{1}$$

where ρ_m, c, T, $\boldsymbol{q}$, $\boldsymbol{j}$, V are the mass density, heat capacity, temperature, heat and electric fluxes and finally voltage. In the previous equation the supradot (˙) denotes time derivative. The entropy balance required to obtain the transport equations is given by [9]:

$$\rho_m \, \dot{s} = -\nabla \cdot \boldsymbol{j}_s + \sigma^s \quad \Rightarrow \quad \begin{cases} \boldsymbol{j}_s = \dfrac{\boldsymbol{q}}{T} \; ; \\[2mm] \sigma^s = \boldsymbol{q} \cdot \nabla\left(\dfrac{1}{T}\right) - \dfrac{1}{T}\, \boldsymbol{j} \cdot \nabla V \end{cases} \tag{2}$$

where $\dot{s}$, $\boldsymbol{j}_s$, σ^s are entropy rate, flux and production, respectively. Note that the entropy production is increased by two factors: thermal conduction and *Joule* heating, the latter electric energy converted into thermal one. From (2) and using the procedure described in [10], the classical transport equations are:

$$\boldsymbol{q} = -\kappa \, \nabla T + \alpha \, T \, \boldsymbol{j} \; ;$$

$$\boldsymbol{j} = -\gamma \, \nabla V - \alpha \, \gamma \, \nabla T \tag{3}$$
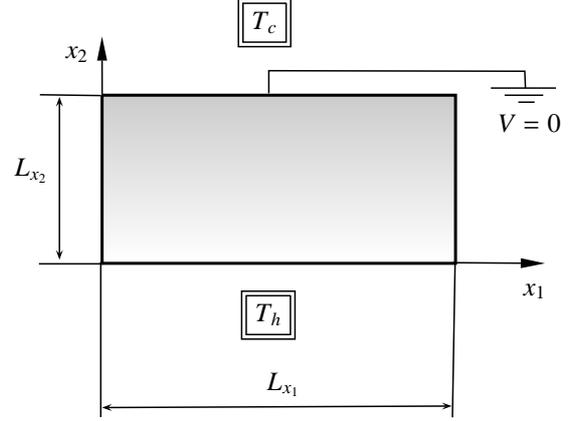

Figure 1: Experimental configuration for the measurement of the *Seebeck* coefficient in thermoelectric photovoltaic materials.

where γ, κ are electric and thermal conductivities and α the *Seebeck* coefficient. These parameters are usually denominated transport properties and, in general, depend on temperature as reported in [11].

As discussed in the introduction, the ENET considers dissipative fluxes $\dot{\boldsymbol{q}}$, $\dot{\boldsymbol{j}}$ in the classical entropy balance (2). Therefore and according to [12], the entropy production becomes:

$$\sigma^s = \boldsymbol{q} \cdot \left[\nabla\left(\frac{1}{T}\right) + \frac{C_1}{T}\, \dot{\boldsymbol{q}} + \frac{C_3}{T}\, \dot{\boldsymbol{j}} \right]$$

$$+ \boldsymbol{j} \cdot \left[-\frac{1}{T}\, \nabla V + \frac{C_2}{T}\, \dot{\boldsymbol{q}} + \frac{C_4}{T}\, \dot{\boldsymbol{j}} \right] \tag{4}$$

where C_1 to C_4 are constants to be determined, closely related with relaxation times. Note that these dissipative fluxes increase the entropy, in other words, add irreversibilities to the thermodynamic system. According to [12], [7], the ENET transport equations are:

$$\boldsymbol{q} = -\kappa \, \nabla T + \alpha \, T \, \boldsymbol{j} - \tau_{qj}\, \alpha \, T \, \gamma \, \nabla \dot{V} + \tau_q \, \kappa \, \nabla \dot{T} \; ;$$

$$\boldsymbol{j} = -\gamma \, \nabla V - \alpha \, \gamma \, \nabla T - \tau_{jq}\, \alpha \, \gamma \, \nabla \dot{T} + \tau_j \, \gamma \, \nabla \dot{V} \tag{5}$$

The direct relaxation times τ_q, τ_j represent thermal and electric "viscosities", closely related with *Cattaneo* [13], [14] and *Drude* [15] models; the coupling relaxation times τ_{qj}, τ_{jq} represent thermal and electric viscosities due to the presence of voltage and of temperature gradients, respectively.

Finally, in order to obtain the thermoelectric governing equations, the boundary conditions are incorpo-
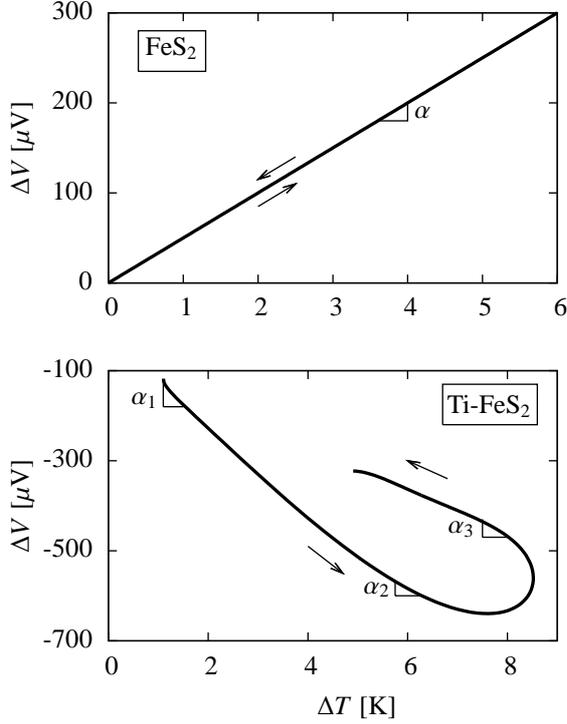
2

Figure 2: Experimental results reported in Ferrer 2006 [1] for FeS$_2$ (top) and Ti-doped FeS$_2$ (bottom) thermoelectric thin films.

rated:

$$Dirichlet: \quad T = \bar{T}, \qquad V = \bar{V}; \tag{6}$$
$$Neumann: \quad \boldsymbol{q} \cdot \mathbf{n} = q_c, \quad \boldsymbol{j} \cdot \mathbf{n} = j_c$$

where $\bar{T}$, $\bar{V}$ are the temperature and voltage, and q_c, j_c the thermal and electric fluxes, all of them prescribed.

3. Physical interpretation of the hysteretic behavior

Before developing a theoretical explanation of the hysteretic behavior using the ENET, the experimental procedure and empirical results reported in [1] are reviewed.

3.1. Experimental procedure

The experimental configuration for the measurement of the *Seebeck* coefficient usually involves placing the thermoelectric between hot T_h and cold T_c faces' temperature and fixing at the latter the voltage, as shown in Figure 1. Considering the classical transport equations (3) and zeroing the prescribed flux $\boldsymbol{j}$, a linear relationship between the applied temperature difference ΔT and

the measured voltage drop ΔV is obtained:

$$\left. \begin{array}{l} \boldsymbol{j} = -\gamma\, \nabla V - \alpha\, \gamma\, \nabla T \\[4pt] \boldsymbol{j} = \mathbf{0} \end{array} \right\} \quad \Rightarrow \quad \Delta V = -\alpha\, \Delta T \tag{7}$$

Note that gradients have been replaced by increments to be in accordance with the experimental measurements. The *Seebeck* coefficient is determined plotting ΔV versus ΔT and calculating the slope α of the linear relationship (7); the sign of α is related to the semiconductor type: n or p.

Two thin-film material samples with dimensions $L_{x_2} = 15$, $L_{x_1} = 25$ [mm] were characterized by the procedure described in the previous paragraph. Two very different results were observed:

- For FeS$_2$, the linear relationship ΔV–ΔT shown in Figure 2 top, with a unique α

- For Ti-doped FeS$_2$, the hysteretic behavior shown in Figure 2 bottom, with different values of α

As discussed in the introduction, for samples that present a hysteretic behavior it is difficult to assign a representative *Seebeck* coefficient: α was calculated from the heating branch in [2] and from the common diagonal slope of different loops obtained applying different ΔT's in [1], fitting the experimental results to a unique α:

$$\Delta V = -\alpha\, \Delta T - \alpha\, K\, \frac{\mathrm{d}(\Delta T)}{\mathrm{d}t} \tag{8}$$

where K was an empirical magnitude with dimension of time. Therefore, the loop shape and its slope, Figure 2 (bottom), were determined by the second and first terms on the right side of (8), respectively.

3.2. Theoretical explanation

The motivation to provide a theoretical explanation using the ENET is due to the dependency of the empirical equation (8) on $\mathrm{d}\Delta T/\mathrm{d}t$ and on K; the two magnitudes can be closely related with those introduced by the ENET: dissipative fluxes and relaxation times.

The relaxation τ_j can be neglected in absence of free electric charges, [7]. From the electric transport equation (5), forcing again $\boldsymbol{j} = \mathbf{0}$:

$$\nabla V = -\alpha\, \nabla T - \alpha\, \tau_{jq}\, \frac{\partial(\nabla T)}{\partial t} \tag{9}$$

Contrasting (8) and (9), the equivalence $K \equiv \tau_{jq}$ is evident. Therefore, the loop shape, i.e. hysteresis, may

depend on τ_{jq}. From a theoretical point of view, the relation between hysteresis and relaxation times already was stated in [6]: this hysteresis depends on the ratio τ_{jq}/t_{ob}, where t_{ob} is the observation time. The ratio depends on the material properties, observing different behaviors if:

$$\tau_{jq}/t_{ob} << 1 \quad \rightarrow \quad \text{Linear response}$$

$$\tau_{jq}/t_{ob} \approx 1 \quad \rightarrow \quad \text{Hysteretical response}$$

Summarizing, from statistical physics it can be said that the microscopic equilibration time τ_{jq} increases when the FeS_2 is doped with Ti, provoking the hysterical behavior.

4. Finite element equations

Several numerical techniques to study the thermo-electric coupling such as the finite difference [16] and the FE methods have been published. The authors of the present work have developed several non-linear FE formulations, see [17], [18], [19], [7]. The first two are steady–state formulations; the third one is dynamic and includes the relaxation time τ_q, permitting the study of hyperbolic propagations of temperature, voltage and thermal flux after the *Cattaneo* model. Finally, the last work presents a complete FE formulation including three relaxation times: τ_q, τ_{qj}, τ_{jq}. These formulations are fully described in the references and therefore will not repeated here.

In the present work, the FE formulation includes the three relaxation times. Since the thermoelectric problem only requires two degrees of freedom per node (temperature and voltage), the assembled FE matrix is:

$$\begin{bmatrix} c_1\mathcal{K}^{TT} + c_2 C^{TT} + c_3 M^{TT} & c_1\mathcal{K}^{TV} + c_2 C^{TV} \\ \\ c_1\mathcal{K}^{VT} + c_2 C^{VT} & c_1\mathcal{K}^{VV} \end{bmatrix} \quad (10)$$

where c_1, c_2, c_3 are time integration parameters and $\mathcal{K}$, C, M the tangent conductivity, capacity and thermal inertia matrices, respectively. Note that $\mathcal{K}$ is denominated stiffness matrix in the *Continuum Mechanics* community; however, for the thermoelectric problem it represents the conductivity matrix. Note also that the coupled matrix will not be symmetric, requiring a special algorithm for the inversion of the assembled matrix.

All terms in the assembled matrix are developed in [19]. In particular, the submatrices C^{VT}, C^{TV} were incorporated in [7] to take into account τ_{jq}, τ_{qj}, respec-

tively:

$$\begin{aligned} C_{AB}^{VT} &= -\tau_{jq} \int_\Omega (\mathcal{B}_A)^{\mathrm{t}} \, \alpha \, \gamma \, \mathcal{B}_B \, \mathrm{d}\Omega \\ \\ C_{AB}^{TV} &= -\tau_{qj} \int_\Omega (\mathcal{B}_A)^{\mathrm{t}} \, T_B \, \alpha \, \gamma \, \mathcal{B}_B \, \mathrm{d}\Omega \end{aligned} \quad (11)$$

where A, B denote two generic global FE nodes, Ω the domain and $\mathcal{B}$ the discretized gradient matrix.

The time-integration algorithm is regularized to avoid *Gibbs* phenomena with the procedure described in [19]. Since the FE formulation was intended to be complete, a three-dimensional isoparametric element is used, although due to geometry and boundary conditions the models are one-dimensional in the present work.

Finally, the FE formulation was implemented into the research code `FEAP` [20], from the University of California at Berkeley. This code provides several dummy routines (user elements) that can be used for the implementation of newly developed modular elements written in the programming language `Fortran`.

5. Calibration of the numerical model: inverse problem

Material properties are required for the numerical simulation of the experiment from [1], but some of these properties were not reported. In addition, the relaxation time is not considered in the experimental work (K is empirically fitted). Therefore, the present numerical model is calibrated with two steps:

1. A Sensitivity Analysis (SA) to identify the thin-film properties that are relevant for the hysteretic behavior

2. An identification IP to, from a single experimental curve, quantify these properties

5.1. Sensitivity Analysis

The objective of the SA is the determination of the relationships between the uncertainties for dependent and independent (or random) variables. The SA is a method for checking the quality of a given model; there are many available procedures to develop a SA and we apply the one from [21]. This procedure uses the concept of Standardized Regression Coefficients (SRC), whose absolute values provide a measure of the importance of each variable, [22].

The dependent variable is a cost function defined as the quadratic difference between the voltage drops obtained from the experimental curve ΔV^{EXP} drawn in

Figure 2 bottom, and from the FE simulation ΔV^{NUM}:

$$f = \frac{1}{N} \sum_{i=1}^{N} \left(\Delta V_i^{EXP} - \Delta V_i^{NUM} \right)^2 \qquad (12)$$

where N is the number of measurement points or FE nodes.

The random variables are defined as the set $\{\alpha, \gamma, \kappa, c, \rho_m, \tau_q, \tau_{jq}\}$ and are assumed to be normally distributed: mean values given in Table 2 are obtained from [23], [1], and standard deviations are assumed to be 25%. These deviations are higher than the usual 10% to take into account a worst-case scenario.

To reduce CPU cost and at the same time guarantee convergence, an optimized sample of size $m = 1000$ was calculated by the procedure developed in [24]. According to this reference, the sample is of the *Latin Hypercube* type since the convergence is faster than the one related with random techniques.
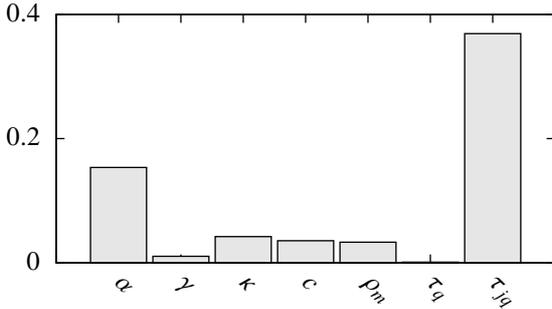

Figure 3: Standardized regression coefficients in absolute value for random variables (material properties).

Figure 3 shows the SRC's in absolute value obtained from the SA. As expected, the cost function is sensitive to the *Seebeck* coefficient α and specially to the relaxation time τ_{jq}. These facts agree with the theoretical assumptions made in Section 3.2: the loop shape and its diagonal slope depend on τ_{jq} and α, respectively. The sensitivities of κ, c, ρ_m are smaller but relevant, since the electric energy generated by the *Seebeck* effects depends on the thermal material properties as will be shown in (14). Finally, the sensitivities of γ, τ_q are not relevant at all, the first due to $j = 0$. The second irrelevancy implies that the purely thermal viscosity is not present in this phenomenon, $\tau_q/t_{ob} << 1$. Consequently, these two random variables will not be considered in the following.

5.2. Inverse problem

The identification IP is directed to evaluate the magnitude of the random variables identified by the SA from a reduced set of data, in particular experimental loops ΔV–ΔT. Note that the material properties taken from the references are not used now, with the objective of characterizing the material without the need of a complete set of experiments. The IP is solved using the procedure described in [24], [25], defining: (i) a set of output variables (parametrization) introduced into the FE code to solve the direct problem, (ii) a cost function and (iii) a minimization method.

Parametrization

In the IP framework, the concept of model parametrization implies the solution characterization sought by a set of parameters, that are the working variables and at the same time the IP output. The choice of the parametrization is often not obvious, a critical step in the problem setup. Here, according to the SA results from Figure 3, the output set is defined as $\{\alpha, \kappa, c, \rho_m, \tau_{jq}\}$. Starting from a wide range of these parameters given by the user, the optimization algorithm searches the optimal values, that must be very similar to the ones taken from the literature.

Cost function

The cost function (12) is redefined as:

$$f^L = \log\left(f + \varepsilon\right) \qquad (13)$$

where $\varepsilon = 10^{-16}$ is a very small non-dimensional value that ensures the function existence when $f \to 0$. According to [26], this redefinition often increases the minimization algorithm convergence.

Minimization

A standard Genetic Algorithm (GA), see [27], is employed to minimize (13) and to obtain the IP output listed in the first column of Table 2. Other optimization techniques such as gradient-based algorithms could be applied, but according to [28] the GA guarantees convergence, whereas gradient-based algorithms strongly depend on the initial guess.

Table 1 first column lists the intrinsic GA parameters. The selected population size permits to find a global op-

Parameter	Value
Population size	30
Crossover ratio	0.8
Mutation ratio	0.02
Number of generations	100

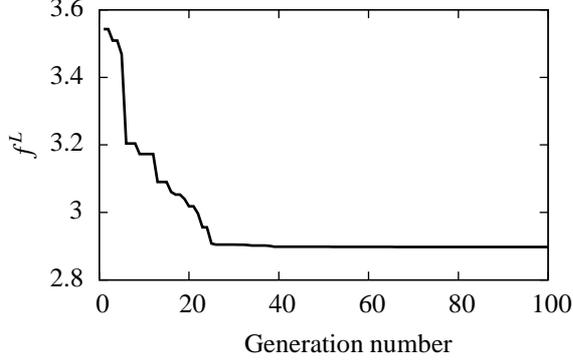Table 1: Parameter values for the genetic algorithm.

Figure 4: Genetic algorithm convergence. Cost function vs. number of generation.

timum with an adequate computational cost. The mutation and crossover parameters are found by trial and error and inject genetic diversity, ensuring that the solution does not fall in a local minima. A large number of generations is chosen to warranty convergence.

5.3. IP results

Figure 4 shows the GA convergence to fit the experimental curve of Figure 5 top (see below), reached with approximately 50 generations and therefore evidencing that the GA parameters from Table 1 were correctly chosen. The IP is repeated ten times to ensure accurate results; the corresponding means and standard deviations are listed in Table 2 second and third columns. Standard deviations are less than 2%, except for the most sensitive parameters α, τ_{jq} with a 3%.

The calculated κ, c, ρ_m are very close to the experimental ones (fourth column). Also, the calculated α, τ_{jq} can be compared with those empirically fitted in [1]. The relative errors between the IP and empirical results are approximately equal to the standard deviations obtained minimizing the problem with GA: the proposed FE-IP combination is suitable for the correct calibration of the material from a single experimental curve.

Para-meter	Mean IP	Standard deviation	Experi-mental	Units
α	-68	3	-65.8	[μV/K]
κ	1.66	1.8	2	[W/mK]
c	534	1.9	547	[J/KgK]
ρ_m	5328	1.3	4900	[Kg/m^3]
τ_{jq}	93	3	93	[s]

Table 2: Means and standard deviations obtained solving ten times the inverse problem for an n-type sample of Ti-doped FeS$_2$. Experimental values taken from [23] except α, τ_{jq} empirically found in [1].
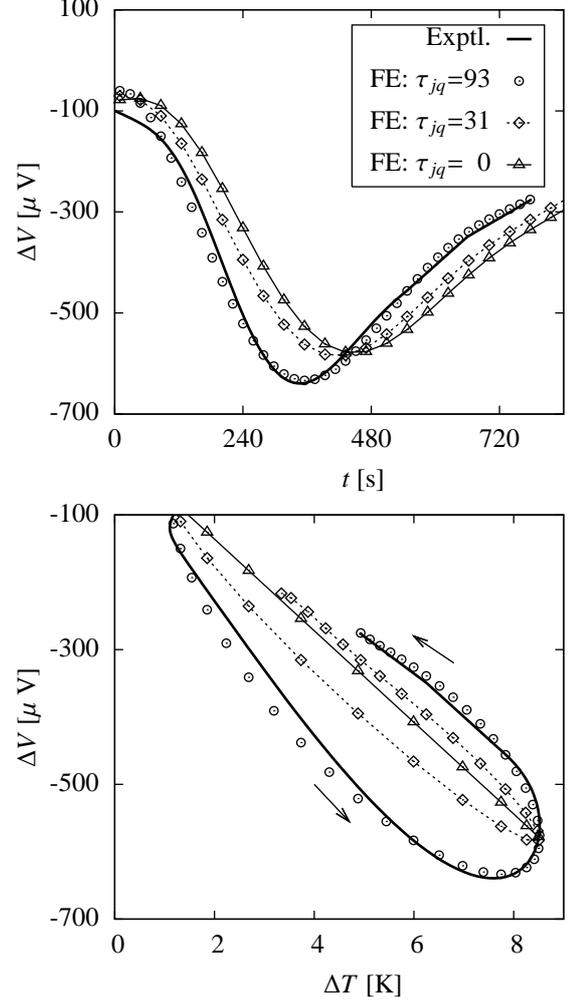

Figure 5: Experimental (thick line) and finite element (symbols) results for three relaxation times, n-type Ti-doped FeS$_2$. Top: voltage drop vs. time, bottom: idem vs. prescribed temperature difference.

From the calculated parameters, FE and experimental responses are compared in Figures 5 for samples of Ti-doped FeS$_2$ of the n–type, in the top ΔV versus time and in the bottom ΔV versus ΔT. The FE model (circles) correctly reproduces the experimental distribution; the only noticeable differences appear at the initial times, for which some error is due to the sharp discontinuity (from $\Delta T = 0$ to 2 [K]) of the initial boundary conditions, see second term on the right side of (9). Smoother initial boundary conditions would fix the problem, but this error is not important for the targeted results.

In the same figure, FE distributions for two different τ_{jq} have also been plotted to study the influence of the relaxation time on the loop shape; as explained before the lower the relaxation the narrower loop, in particu-
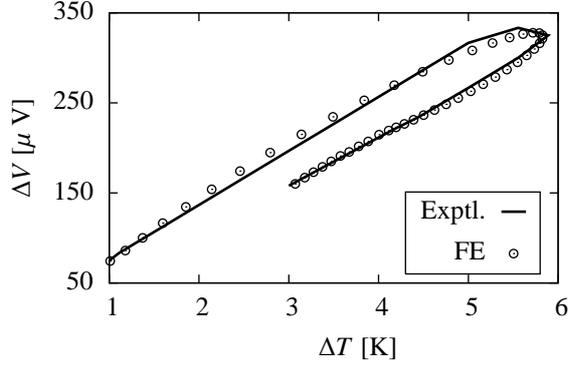
6

Figure 6: Experimental (solid line) and finite element (circles) results for a p-type sample of Ti-doped FeS_2. Measured voltage drop vs. applied temperature difference.
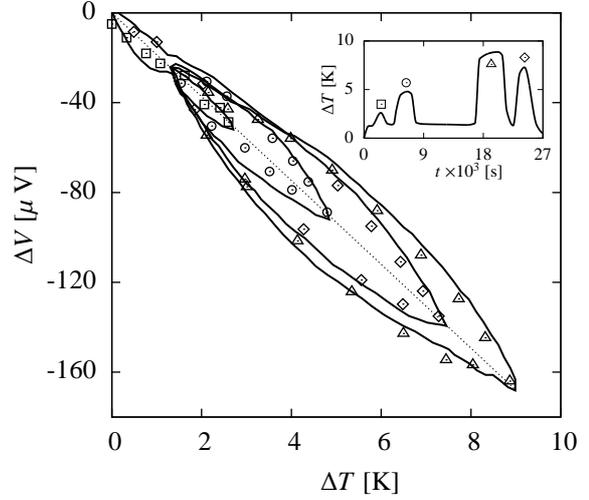

Figure 7: Experimental (solid line) and finite element (symbol for each peak) results for n-type sample of FeS_2. Measured voltage drop vs. applied temperature difference for four different peaks.

lar there is no hysteresis if $\tau_{jq} = 0$. Although no experimental comparisons are available, the distributions when τ_{jq} decreases imply that the error at initial times is mitigated. This fact is again due to the second term on the right side of (9): the smaller τ_{jq} the less influent this term is.

Figure 6 shows the same comparison but for a p-type Ti-doping; the agreement between experimental and numerical loops is again very good. Ten IP cases have been executed to recalculate the material properties, obtaining the same κ, c, ρ_m but different $\alpha = 55.5$ [μV/K], $\tau_{jq} = 30.6$ [s], probably due to a difference in the doping process. No comparison is given here since no values are reported. The *Seebeck* coefficient changes sign due to the p-type doping and its value is smaller, hinting the lower performance of this material. The value of τ_{jq} is about one third, reflecting the narrowness of the loop with respect to that of Figure 5. This reduction is also detrimental since from (9) it can be observed that the higher the relaxation time the higher the voltage drop.

The FE-IP combination is now used to characterize two new samples from [1], executing again ten IP's and obtaining values:

- for a PdS sample a calculated $\alpha = -350 \pm 32$ [μV/K], same order as the experimental -300±40 reported in [29]

- for an n-type FeS_2 sample a calculated $\alpha = -18 \pm 3$ [μV/K] again close to the experimental $\alpha = -19$, measured in [1].

The calculated relaxation times for both samples are $\tau_{jq} = 30, 102$ [s], not measured in the references.

Finally, a more complete experiment from [1] for the second sample is numerically reproduced in Figure 7: a non–regular ΔT versus time signal is applied and the

voltage drop is measured. Four pulses of different bandwidth and amplitude are prescribed (upper right) producing four loops (main figure). The objective of this experiment was to show that all loops have a common slope α, making possible its measurement. It is important to remark that to accurately replicate the experiment, a careful data reading with a smoothing technique of the slopes and amplitudes is necessary. Four different symbols are used to differentiate the four loops and the agreement is again very good, not only for the four loops but also for the way–in and way–out curves.

6. Design of experiments for the validation of the theoretical explanation

The aim of this section is to present three numerical experiments that could be experimentally performed in the future to further validate the theoretical explanation for the hysteretic behavior. From the energy balance (1) and transport equations (5), and assuming $\boldsymbol{j} = \boldsymbol{0}$, $\tau_q = 0$ as before, the following *Poisson* equation is obtained:

$$\nabla^2 V = -\alpha \frac{\rho_m c}{\kappa} \dot{T} - \tau_{jq} \alpha \frac{\rho_m c}{\kappa} \ddot{T} \qquad (14)$$

In (14), the sources (terms on the right side) depend on the material properties α, κ, ρ_m, c, on temperature derivatives $\dot{T}$, $\ddot{T}$ and on the relaxation time, τ_{jq}; according to the proposed explanation:

$$\boxed{\tau_{jq} = 0 \quad \text{or} \quad \ddot{T} = 0 \quad \Rightarrow \quad \text{No hysteresis}}$$
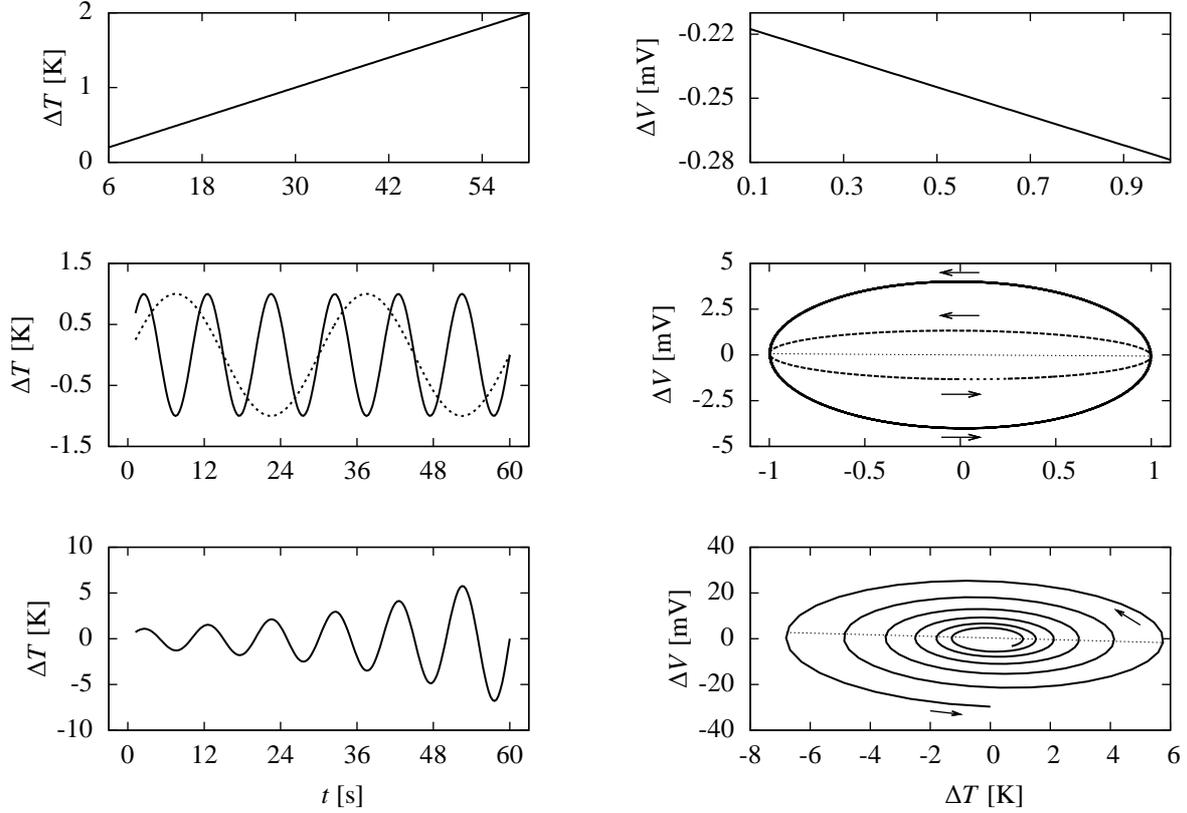
Figure 8: Proposed numerical experiment temperature increment signals vs. time (left) and resulting voltage drop vs. difference temperature (right) for an n-type sample of Ti-doped FeS$_2$. Applied signals: linear (top), sinusoidals (middle) and exponentially increasing (bottom). For middle figure, frequencies $\omega = 4\pi/\hat{t}$ continuous line, $12\pi/\hat{t}$, dashed. Only finite element results shown.

As already verified, there will be no hysteretic behavior if $\tau_{jq} = 0$. To check the absence of hysteresis when the prescribed signal is so that $\ddot{T} \equiv \mathrm{d}^2(\Delta T)/\mathrm{d}t^2 = 0$, three numerical cases are performed in the following subsections. In all of them, the simulation is done with the FE, studying an n-type sample of Ti-doped FeS$_2$ material.

6.1. Case **A**

The signal is forced to have $\ddot{T} = 0$ with a linear T shown in Figure 8 top left. A completely linear response without any hysteresis is obtained when ΔV is plotted versus ΔT as in the top right, and its slope is the unique α value. Therefore, an alternative for the proper characterization of the *Seebeck* coefficient of these materials would be to apply a $\ddot{T} = 0$ signal and use the classical relation (7).

6.2. Case **B**

In this case, the influence of the frequency is studied; two sinusoidal T-signals with the same amplitude but

different frequencies $\omega = 4\pi/\hat{t}$, $12\pi/\hat{t}$ are prescribed as in Figure 8 middle left. The signal is applied up to an arbitrary time of 60 [s]. The middle right figure shows two recurrent and superimposed hysteretic ellipses for each of the periods. For both frequencies, hysteretic behaviors are observed, since $\tau_{jq} \neq 0$ and $\ddot{T} \neq 0$. Three interesting remarks can be made:

- At $\Delta T = \pm 1$ [K], the voltage drop for the two signals is equal, since for both $\ddot{T} = 0$

- At $\Delta T = 0$ [K] the difference between ellipse heights is maximum, since $\ddot{T}$ is also maximum

- The increase of voltage drop (ellipse height) is proportional to the signal frequency since $\ddot{T} \propto \omega^2$

The last remark confirms, as was argued in [5], that the influence of relaxation times is stronger for fast effects such as ultrasound waves. For these concentric ellipses, α could be obtained geometrically measuring their common slopes, as in [1].

8

6.2.1. Case C

The influence of the T-signal amplitude is studied in this case. An exponentially increasing sinusoidal signal is applied, as in Figure 8 bottom left. The response, bottom right, is a growing spiral centered at the origin. The distance between two branches is proportional to the time between two consecutive signal periods.

Again the slope of the symmetry axis gives the *Seebeck* coefficient. Given that the same material is simulated, the three slopes of the right figures are equal, although they look different due to the different scale.

7. Conclusions

This work presents a theoretical explanation for the understanding of the hysteretic behavior in thin-film photovoltaic materials, using the extended non-equilibrium thermodynamics. It is concluded that the hysteresis depends on the relaxation time τ_{jq} and on the acceleration of the prescribed temperature $\ddot{T}$. The latter dependency could explain the strong influence of relaxation times on fast effects such as ultrasonic waves. Experimental cases from the literature have been simulated using a finite element formulation developed by the authors in previous publications, validating the theoretical explanation. Three numerical cases have been proposed and simulated to fully validate in the future our theoretical explanation with laboratory experiments.

In addition, an identification inverse problem has also been performed for the characterization of the *Seebeck* coefficient and of the relaxation time τ_{jq} along with other relevant material properties. The combination of the inverse problem and of the finite element method permits a good characterization of thin-film material properties from a single experimental curve.

8. Acknowledgments

9. References

[1] I.J. Ferrer, P. Díaz-Chao, A. Pascual, and C. Sánchez. Hysteresis-like behaviour of the thermoelectric voltage in photovoltaic materials. *Thin Solid Films*, 511-512:177–181, 2006.

[2] D. Galushko, N. Ermakov, M. Karpovski, A. Palevski, J.S. Ishay, and D.J. Bergman. Electrical, thermoelectric and thermophysical properties of hornet cuticle. *Semiconductor Science and Technology*, 20:286–289, 2005.

[3] M. Plotkin, I. Hod, A. Zaban, S.A. Boden, D.M. Bagnall, D. Galushko, and D.J. Bergman. Solar energy harvesting in the epicuticle of the oriental hornet (Vespa Orientalis). *Naturwissenschaften*, 97:1067–1076, 2010.

[4] A.R. Varrenti, C. Zhou, A.G. Klock, S.H. Chyung, J. Long, S.O. Memik, and M. Grayson. Thermal sensing with lithographically patterned bimetallic thin-film thermocouples. *IEEE Electron Device Letters*, 32:818–820, 2011.

[5] D. Jou and G. Lebon. *Extended Irreversible Thermodynamics*. Springer-Verlag Berlin Heidelberg, 1996.

[6] E. Hernández-Lemus and E. Orgaz. Hysteresis in nonequilibrium steady states: the role of dissipative couplings. *Revista Mexicana de Física*, 48:38–45, 2002.

[7] R. Palma. *Thermodynamic Formulation for Non-linear Finite Element Applied to Multicoupled Materials*. PhD thesis, University of Granada, 2012.

[8] S.R. de Groot and P. Mazur. *Non-equilibrium Thermodynamics*. Dover, 1984.

[9] R.Y. Nuwayhid, F. Moukalled, and N. Noueihed. On entropy generation in thermoelectric devices. *Energy Conversion and Management*, 41:891–914, 2000.

[10] H.B. Callen. *Thermodynamics and an Introduction to Thermostatics*. John Wiley and Sons, Inc, 1985.

[11] D.M. Rowe, editor. *CRC Handbook of Thermoelectrics*. CRC Press, 1995.

[12] J.E. Llebot, D. Jou, and J. Casas-Vázquez. A thermodynamic approach to heat and electric conduction in solids. *Physica*, 121(A):552–562, 1983.

[13] C. Cattaneo. On heat conduction (in Italian). *Atti Seminario Mat. Fis. University Modena*, 3:83–1013, 1938.

[14] H. Rahideh, P. Malekzadeh, and M.R. Golbahar. Heat conduction analysis of multi-layered FGMs considering the finite heat wave speed. *Energy Conversion and Management*, 55:14–19, 2012.

[15] P. Drude. On electrical theory for metals and on galvanomagnetic and thermomagnetic effects (in German). *Annalen der Physik*, 308:369, 1900.

[16] A. Rodríguez, D. Astrain, and A. Martínez. Study of thermoelectric systems applied to electric power generation. *Energy Conversion and Management*, 50:1236–1243, 2009.

[17] J.L. Pérez-Aparicio, R.L. Taylor, and D. Gavela. Finite element analysis of nonlinear fully coupled thermoelectric materials. *Computational Mechanics*, 40:35–45, 2007.

[18] J.L. Pérez-Aparicio, R. Palma, and R.L. Taylor. Finite element analysis and material sensitivity of Peltier thermoelectric cells coolers. *International Journal of Heat and Mass Transfer*, 55:1363–1374, 2012.

[19] R. Palma, J.L. Pérez-Aparicio, and R.L. Taylor. Non–linear finite element formulation applied to thermoelectric materials under hyperbolic heat conduction model. *Computer Method in Applied Mechanics and Engineering*, 213:93–103, 2012.

[20] R.L. Taylor. *FEAP A Finite Element Analysis Program: User Manual*. University of California, Berkeley, 2010. http://www.ce.berkeley.edu/feap.

[21] P. Hoes, M. Trcka, J.L.M. Hensen, and B.H. Bonnema. Investigating the potential of a novel low-energy house concept with hybrid adaptable thermal storage. *Energy Conversion and Management*, 52:2442–2447, 2011.

[22] I.P. Koronaki, E. Rogdakis, and T. Kakatsiou. Thermodynamic analysis of an open cycle solid desiccant cooling system using artificial neural network. *Energy Conversion and Management*, http://dx.doi.org/10.1016/j.enconman.2012.01.022, 2012.

[23] K. Kato, Y. Okamoto, J. Morimoto, and T. Miyakawa. The thermoelectric properties of FeS_2. *Journal of Materials Science Letters*, 16:914–916, 1997.

[24] R. Palma, G. Rus, and R. Gallego. Probabilistic inverse problem and system uncertainties for damage detection in piezoelectrics. *Mechanics of Materials*, 41:1000–1016, 2009.

[25] J. Zhao, Y. Song, W. Lam, W. Liu, Y. Liu, Y. Zhang, and D. Wang. Solar radiation transfer and performance analysis of an optimum photovoltaic/thermal system. *Energy Conversion and Management*, 52:1343–1353, 2011.

[26] R. Gallego and G. Rus. Identification of cracks and cavities using the topological sensitivity boundary integral equation. *Computational Mechanics*, 33:154–163, 2004.

[27] O.E. Canyurt and H.K. Ozturk. Three different applications of genetic algorithm (GA) search techniques on oil demand estimation. *Energy Conversion and Management*, 47:3138–3148, 2006.

[28] G. Rus, R. Palma, and J.L. Pérez-Aparicio. Optimal measurement setup for damage detection in piezoelectric plates. *International Journal of Engineering Science*, 47:554–572, 2009.

[29] I.J. Ferrer, P. Díaz-Chao, A. Pascual, and C. Sánchez. An investigation on palladium sulphide (PdS) thin films as a photovoltaic material. *Thin Solid Films*, 515:5783–5786, 2007.